PHYSICAL REVIEW E **102**, 013306 (2020)

Mesoscopic method to study water flow in nanochannels with different wettability

Tao Zhang,[1,2,*] Farzam Javadpour,[2,†] Xiangfang Li,[1] Keliu Wu,[1,3] Jing Li,[3] and Ying Yin[4]

[1]*Key Laboratory for Petroleum Engineering of the Ministry of Education, China University of Petroleum, Beijing 102249, China*
[2]*Bureau of Economic Geology, Jackson School of Geosciences, The University of Texas at Austin, University Station, Box X, Austin, Texas 78713, USA*
[3]*The Department of Chemical and Petroleum Engineering, University of Calgary, Alberta, Canada T2N1N4*
[4]*MOE Key Laboratory of Thermo-Fluid Science and Engineering, School of Energy and Power Engineering, Xi'an Jiaotong University, Xi'an 710049, China*

(Received 9 April 2020; revised 9 June 2020; accepted 15 June 2020; published 9 July 2020)

Molecular dynamics (MD) simulations is currently the most popular and credible tool to model water flow in nanoscale where the conventional continuum equations break down due to the dominance of fluid-surface interactions. However, current MD simulations are computationally challenging for the water flow in complex tube geometries or a network of nanopores, e.g., membrane, shale matrix, and aquaporins. We present a novel mesoscopic lattice Boltzmann method (LBM) for capturing fluctuated density distribution and a nonparabolic velocity profile of water flow through nanochannels. We incorporated molecular interactions between water and the solid inner wall into LBM formulations. Details of the molecular interactions were translated into true and apparent slippage, which were both correlated to the surface wettability, e.g., contact angle. Our proposed LBM was tested against 47 published cases of water flow through infinite-length nanochannels made of different materials and dimensions–flow rates as high as seven orders of magnitude when compared with predictions of the classical no-slip Hagen-Poiseuille (HP) flow. Using the developed LBM model, we also studied water flow through finite-length nanochannels with tube entrance and exit effects. Results were found to be in good agreement with 44 published finite-length cases in the literature. The proposed LBM model is nearly as accurate as MD simulations for a nanochannel, while being computationally efficient enough to allow implications for much larger and more complex geometrical nanostructures.

DOI: 10.1103/PhysRevE.102.013306

I. INTRODUCTION

Water flow at the nanoscale, which is relevant to multiple scientific disciplines, has tremendous implications in diverse technological applications, including water desalination [1], energy harvesting and conversion [2], development of biochemical nanosensors [3], drug delivery across biological cell membranes [4], and hydraulic fracturing of unconventional shale gas and tight oil reservoirs [5,6]. Perturbed by the interactions between water and solids, the transport behavior of water molecules in nanoscale geometries differs significantly from that observed in the pipe flow [7,8]. From the early 2000s, intense research has been implemented both experimentally and theoretically by researchers to explain and characterize the structural, thermodynamic, and transport properties of water confined in nanoscale geometries. However, the robust modeling of the process in complex geometrical nanostructures at laboratory or prototype scales remain out of reach.

Dominated by the high ratio of wall surface area to volume, many investigations indicate that properties of nanoconfined water differ significantly from those of bulk water [7–12]. Because of the presence of wall-force-field interactions (mainly van der Waals and Coulomb-type interactive forces), mass density distribution is structured and layered in both hydrophilic and hydrophobic systems, resulting in spatially varying shear-stress fields and density-dependent fluid-velocity distributions [10,13,14]. Moreover, different kinds of boundary conditions, such as slip, no-slip, or even stick, are all possible at the water-solid interface, which depends on the strength of the interactions between water molecules and solid surfaces [15–19]. As a result, huge differences and contradictions, from flow reduction to flow enhancement with several orders of magnitude over continuum fluid theory, are commonly found in the literature [9]. A conventional macroscopic method, which is based on Navier-Stokes equations with a no-slip boundary, seems to be inadequate to model water flow in such situations [20,21].

In addition to experiments, MD simulations are widely used to model water confined flow [22]. Not only does MD provide instantaneous calculation results, but it can also help to perform sensitivity studies of the controlling parameters hardly feasible by experiments. MD simulation has the advantages of accuracy and popularity, and extensive fluid flow investigations using MD have thus been conducted on a single nanochannel [23–28] or networks of interconnected nanopores [29–34]. However, the scales of these MD simulations are usually below 100 nm, and the huge computational requirements of MD simulation make it impractical for many engineering applications. For example, membranes that have

---

[*] tobiascheuing@163.com
[†] farzam.javadpour@beg.utexas.edu

a micrometer to millimeter thickness scale are too large to be treated by MD simulations [4,35]. Even using a supercomputer having thousands of processors, researchers require several weeks to run the simulations, presenting challenges to an engineering fabrication of commercial membranes [22,36,37].

Here, we present a novel LBM for confined water flow, a mesoscopic method lying between microscopic (molecule) and macroscopic (continuum) scales. Far from being a mere technicality, this method creates an opportunity for simulating confined water flow in large space and timescales with less computational demand, easily applicable complex systems such as biological membrane and tight oil and shale gas reservoirs. With this method, the interactions between water-solid and water-water molecules can be modeled by utilizing the forces balance between group of molecules, rather than tracking individual molecules. We show how powerful this method can be by simulating water flow through nanochannels of infinite length (periodic boundary conditions) and finite length (with entrance and exit effects), and we show how our results are in accord with most cases in different investigations. The method cannot be applied to simulate water transport in nanochannels having dimensions smaller than 1.6 nm, where momentum-transport is controlled by individual molecules rather than a group of molecules [38,39].

II. METHODS

The evolution equation in the lattice Boltzmann frame, a minimally discrete version of the Boltzmann equation, can be expressed as [40]

$$f_i(\mathbf{x}+\mathbf{e}_i\Delta t, t+\Delta t) - f_i(\mathbf{x},t) = -\frac{1}{\tau}\left[f_i(\mathbf{x},t) - f_i^{\mathrm{eq}}(\mathbf{x},t)\right], \tag{1}$$

where $f_i(\mathbf{x},t)$ is the probability density function, indicating a particle with velocity $\mathbf{e}_i$ at position $\mathbf{x}$ and time t. The left side of the equation represents stream, whereas the right side stands for collisional interactions; Δt is a time step, $f^{\mathrm{eq}}(\mathbf{x},t)$ is the equilibrium distribution function, and τ is the mean collision time, written as

$$\tau = \frac{\upsilon_e}{c_s^2\Delta t} + 0.5, \tag{2}$$

where υ_e is kinematic viscosity, c_s is sound speed, and $c_s = 1/\sqrt{3}$ for the D2Q9 lattice model. In this work, the most widely used D2Q9 lattice model for 2D space was adopted for its simplicity and efficiency. The D3Q19 lattice model can be used to easily extend the simulation into 3D space [41]. Lattice discrete velocity $\mathbf{e}_i$ is related to the particular velocity model. The D2Q9 lattice model is given by

$$\mathbf{e}_i = \begin{cases} 0, & i=0 \\ \left(\cos\left[\frac{(i-1)\pi}{2}\right], \sin\left[\frac{(i-1)\pi}{2}\right]\right), & i = 1 \sim 4. \\ \sqrt{2}\left(\cos\left[\frac{(i-5)\pi}{2}+\frac{\pi}{4}\right], \sin\left[\frac{(i-5)\pi}{2}+\frac{\pi}{4}\right]\right), & i = 5 \sim 8 \end{cases} \tag{3}$$

In the standard D2Q9 pattern, the equilibrium distribution function f^{eq} is defined as

$$f_i^{\mathrm{eq}} = \omega_i\rho\left[1 + \frac{1}{{c_s}^2}(\mathbf{e}_i\cdot\mathbf{u}) + \frac{1}{2{c_s}^4}(\mathbf{e}_i\cdot\mathbf{u})^2 - \frac{1}{2{c_s}^4}\mathbf{u}^2\right], \tag{4}$$

where w_i is the weighting factor. Here, $w_0 = 4/9$ for $i = 0$, $w_i = 1/9$ for $i = 1{-}4$, and $w_i = 1/36$ for $i = 5{-}8$.

Accordingly, macroscopic fluid density ρ and velocity $\mathbf{u}$ are determined by

$$\rho = \sum_i f_i, \quad \text{and} \quad \rho\mathbf{u} = \sum_i f_i\mathbf{e}_i. \tag{5}$$

The external force $\mathbf{F}$ is incorporated into the LB frame by adding velocity increment $\delta\mathbf{u} = \tau\mathbf{F}/\rho$ to macroscopic velocity $\mathbf{u}$. Each time iteration of these governing equations proceeds in three steps: first, particle distributions stream to nodes $f_i(\mathbf{x},t)$. Second, macroscopic parameters such as density and velocity are obtained by these new distribution functions. Finally, the equilibrium distribution function is calculated and particle distribution undergoes collision. The program then goes into the next loop for a new $f_i(\mathbf{x}+\mathbf{e}_i\Delta t, t+\Delta t)$.

III. RESULTS

A. LBM for water flow through nanochannels

The body of work indicating that conventional no-slip Poiseuille flow is not suitable for use in confined water flow for both hydrophobic and hydrophilic cases is considerable [35,42,43]. The reason lies in the relative strength of water-solid interactions and water-water interactions, which makes the no-slip boundary condition unacceptable. Generally, for confined water in hydrophilic nanochannels, the attraction force between water-solid molecules is much stronger than that of water-water interactions, and a substantial epitaxial ordering of water molecules must be induced [44]. This ordering brings about a notable increase in the density and viscosity of the near-wall water, in which a solidlike state exists instead of a viscous, liquidlike state for the bulk water, reducing effective pore size [45]. The phenomenon is called *multilayer sticking*, in which no slip is observed [46] [Fig. 1(a)]. In contrast, in the hydrophobic nanochannel, the attraction force between water-solid molecules is smaller than that of water-water interactions. It is entropically unfavorable for the hydrophobic surface to bind water molecules by hydrogen bonds, and a depletion region having low density and viscosity can be found approaching the wall surface, as in a liquid-vapor interface [47]. Additionally, water molecules can move/slide directly along wall surfaces (velocity *jump* at walls), giving rise to a positive slip length [48]. The assumption of a no-slip boundary is invalid, displaying low friction of water inside the channel [Fig. 1(c)]. Between these two situations, a transition status exists [Fig. 1(b)], in which the no-slip boundary remains valid, although the density and viscosity of water near walls is decreased slightly.

The true slip length $l_{s,t}$, also called *partial slip length* [Fig. 1(c)], is defined by the ratio of slip velocity to strain rate in the position of the effective hydrodynamic boundary [9,49]. In addition, the influences of radially varied density and viscosity on the flow are further represented by the so-called *apparent slip length* $l_{s,a}$ [50]. More details on the flow mechanisms can be found in our previous study (Wu *et al.* [51]). The key to modeling confined water flow accurately involves characterization of the two parameters reliably.

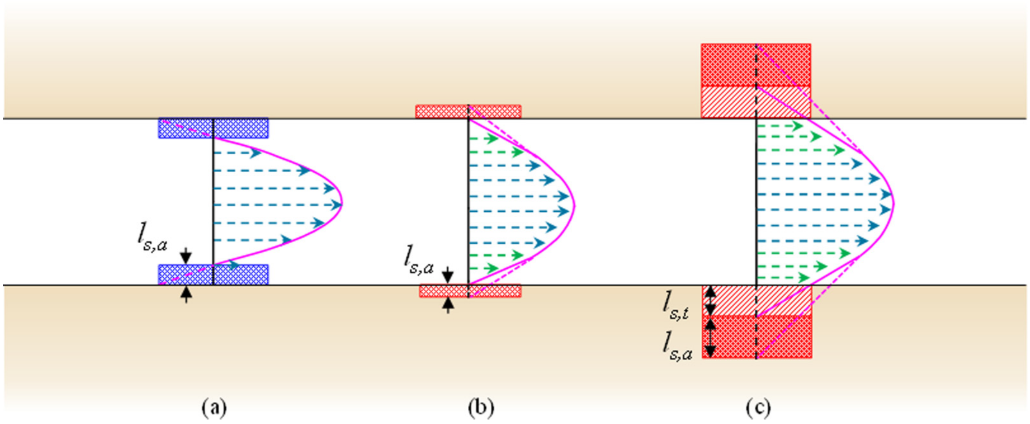

FIG. 1. Schematic diagram of water flow in a nanochannel [51]. The strength of the water-solid attraction weakens from (a) (hydrophilic) to (c) (hydrophobic). (a) The water-solid interaction is larger than the water-water interaction. The density and viscosity of the blue-square region is higher than the water in the bulk-water region, inducing a negative apparent slip length $l_{s,a}$. (b) The water-solid interaction is comparable to the water-water interaction. The density and viscosity of the green-arrow region is smaller than that of the bulk-water region (green arrows), owing to depletion. Apparent slip $l_{s,a}$ occurs too, but the value is positive. (c) The water-solid interaction is smaller than the water-water interaction. Similar to B, the density and viscosity of the green-arrow region is smaller than that of the bulk-water region (with green arrows.) In addition to the apparent slip $l_{s,a}$ induced by density and viscosity, the true slip $l_{s,t}$ occurs owing to the direct surface sliding of water molecules on the wall. Both of the two slip-length values are positive here.

1. True slip

In the LB frame, a linear combination of bounceback and specular reflection, commonly used in modeling of gas slippage [52,53], is revisited to capture the true slip length of water near the solid boundary. That is, when a particle-density distribution function f_i hits a wall surface, it will be bounced back with probability χ, and be specularly reflected with probability $(1-\chi)$, shown as [54]

$$f_i = \chi f_i^{\mathrm{bb}} + (1-\chi) f_i^{\mathrm{sr}}, \qquad (6)$$

where χ is the accommodation coefficient, f_i^{bb} is the bounceback distribution function, and f_i^{sr} is the specular reflection distribution function. Note that this equation is a basic lattice implementation of the idea of kinetic boundary condition proposed by Maxwell, which can be traced back to 1879 [55]. According to the Navier linear-slip model, the following expression can be used to connect the accommodation coefficient χ with true slip length $l_{s,t}$ [56–58]:

$$\chi = \left(1 + \frac{l_{s,t} + \left[\frac{1}{4} - \frac{2}{3}(\tau - 0.5)^2\right]\frac{1}{N_y}}{\tau - 0.5}\right)^{-1}, \qquad (7)$$

where τ is mean collision time with a value of 1.11 (Appendix A) and N_y is lattice grid numbers in the radial direction. Before the true slip length $l_{s,t}$ is incorporated into Eq. (7), the physical unit should be changed into lattice units (Appendix B).

True slip length prediction is affected by many factors, such as wall smoothness [59], temperature [60], and viscosity [61]. Apart from these factors, the related factors in experimental measurements also include dissolved gas at walls [62], operational conditions [63], and unknown contaminants [64]. However, on an ideal, atomically smooth surface, true slip length depends on the nature of water-solid interactions and water-water interactions [65]. Fortunately, an ideal system involving water-solid interactions can be readily created using MD simulations, leading to the possibility of a description of the interactions through calculation of trajectories of individual molecules, and the empirically derived potentials can be sufficient to characterize the interactions quite well [19]. Specifically, for characterizing these interactions, an expression of water true-slip length related to contact angle can be described by a simple quasiuniversal relationship [66]:

$$l_{s,t} = C(\cos\theta + 1)^{-2}, \qquad (8)$$

where θ is the contact angle, coefficient C is obtained from a fit with MD simulations data, and it equals 0.63 [43]. This value remains a constant value (= 0.63) in all the simulation runs. Here the strength of the interaction is described by the contact angle or wettability. Note that for few materials, such as boron nitride, true slip length $l_{s,t}$ is not completely controlled by wetting properties, although most nanochannels support this general relationship, and the detail introduction of the relationship between the true slip length and the wall wettability can be found in Wu *et al.* [51]. Thus, attention should be paid when using this equation.

2. Apparent slip

Effective slip length can be extremely large—as much as 68 μm [42]—although in some reported confined systems it drops to a negative value [67]. Therefore, in addition to the true slip which is always a positive value, apparent slip induced by density variation is the possible phenomenon for the reportedly wide range of slip length data [51]. In the confined situation, breakdown of uniform fluid density is a widely reported behavior as a result of water-solid interactions [68]. Exerted by an extremely large atomic repulsion, the first liquid layer begins to develop after a void region near the surface [69] [Fig. 2(a)]. Then density profiles begin to exhibit strong oscillations in the number of water molecules in the layers adjacent to the wall surface, these oscillations

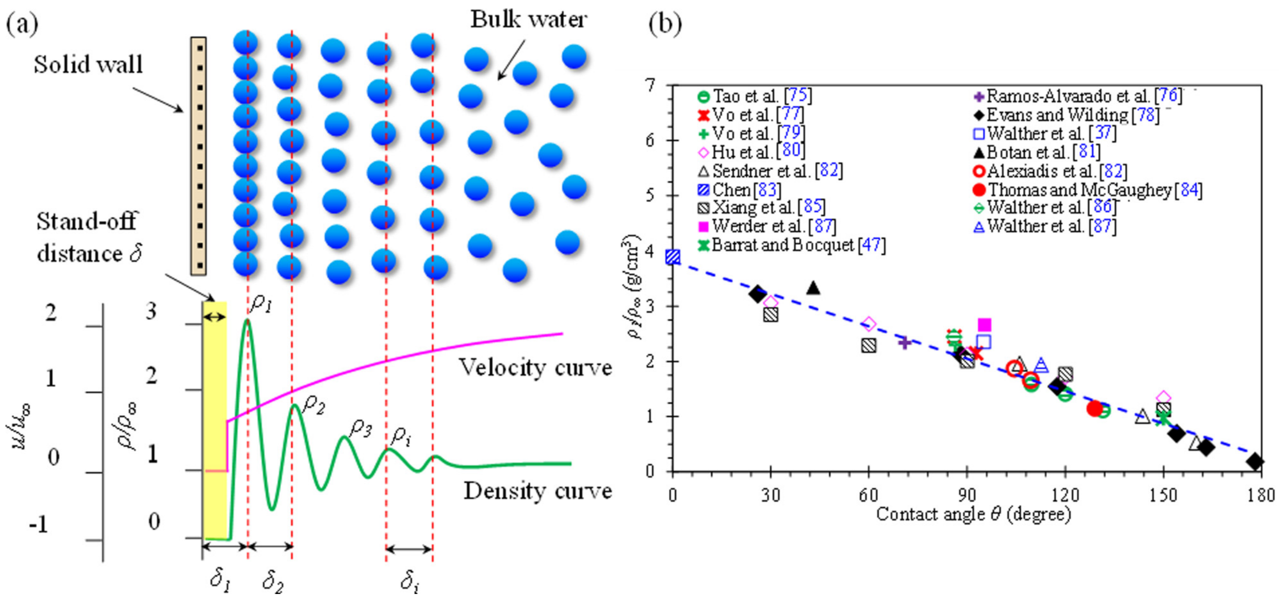

FIG. 2. (a) Typical representation of water molecules near the wall surface in a nanochannel (>1.60 nm) [74]. Water molecules (blue circles) tend to be layered and ordered near the wall surface. The fluctuating green curve is the water-density profile. The first liquid layer starts to develop after the yellow-filled region near the wall surface. The term δ_1 is defined as the distance between the solid surface and the location of the first density peak, and δ_2 is defined as the distance between the location of the first density peak and the second density peak. The value of stand-off distance δ is generally taken as 0.24 nm for water, and δ_1 as well as δ_2 are about one molecular diameter, 0.28 nm for water (Appendix C). The pink curve is the velocity profile, and no velocity can be observed within the stand-off distance because water density is zero in the region. (b) Determination of the relationship between the first density peak and the contact angle. Data are from MD simulations in the literature [37,43,47,75–88]. Detailed parameters shown in Appendix F. Blue dashed line is optimally fitted curve.

gradually decaying and converging in the bulk region [70]. This density inhomogeneity leads to spatially inhomogeneous viscosity, affecting flow behavior in the form of apparent slip [69].

Velocity within the void region is not well defined [Fig. 2(a)] because water density rapidly reaches zero in that region, whereas a sharp velocity increase can be observed in the first density layer, exhibiting a slip [71]. Water molecules are apparently sliding on the cavity, much like a magnetically levitated train on its pathway, displaying ultralow water-solid friction and significant flow enhancement [72]. This could be the origin of the true slip length, as discussed earlier; therefore, the location of the slip plane is actually δ away from the wall surface. The term δ is called the *stand-off distance*, which is defined as the distance between the solid surface and the location where water density appears, and the true slip length mentioned earlier is defined as δ away from the wall. Given these physically reasoned observations, the effective transport diameter can be defined as $d_e = d - 2\delta$. In other words, the stand-off distance should thus be excluded in calculating the effective transport diameter. Note that a small variation in tube diameter may cause considerable deviation in the prediction of volumetric flow rate because flow rate depends on the third power of the diameter [44,47,73].

The water density in the near-wall region is also strongly affected by interactions from the wall surface [89]. Given the MD simulation results [Fig. 2(b)], the first peak density and contact angle are correlated as a simple linear relationship:

$$\rho_1/\rho_\infty = 3.808 - 0.2\theta, \tag{9}$$

where ρ_∞ is density in the bulk region. Several points need to be clarified. First, the first peak density decreases as the contact angle increases, which appears to be related to decrease of the molecular dipole moment and weakening of hydrogen bonding at the wall surface [90]. Second, as captured by Eq. (9), the first peak density is larger than that of the bulk region in the hydrophilic condition [72,83,85], whereas its value can be smaller than the density in the bulk region in the superhydrophobic condition [43,78]. That is to say, no maximum/peak density exists in the density profile, which is similar to the density-profile case of the air-liquid interface [61]. Third, when the channel height is less than 1.6 nm, the density profile is not well defined, and the first peak density closely depends on channel height [61,91], making application of Eq. (9) inappropriate in these small channels. Forth, although water models from the different MD simulations might result in different absolute values of density, viscosity and other properties, the dimensionless density (ρ_1/ρ_∞), which characterizes the relative interactions between water-water molecules and water-solid molecules, is independent of the water model selection at a specific wettability. Finally, only the density of the first peak point is used here as the characterization parameter to describe the influence of wettability on the density structure. In fact, the whole density profile will change with the variation in surface wettability, which can be properly captured in the following LB frame.

Compared with those of thermodynamic-equilibrium density, structuring and layering effects lead to a different effective density value, altering dynamic viscosity and diffusion coefficients in confined transport behavior [45]. As mentioned earlier, inhomogeneous density results from relative interactions between water-solid and water-water. In LBM, water-water interactions, originally proposed by Shan and Chen [92], are introduced as a mean field-body force between nearest particles and are expressed as

$$\mathbf{F}_b(\mathbf{x},t) = -G_b\psi(\mathbf{x},t)\sum_i \omega_i\psi(\mathbf{x}+\mathbf{e}_i\Delta t,t)\mathbf{e}_i, \qquad (10)$$

where ω_i is equilibrium weight, $\psi(\mathbf{x},t)$ is a phenomenological pseudopotential (also called *generalized density*), $\psi(\mathbf{x},t) = 1-\exp(-\rho/\rho_0)$, and reference density $\rho_0 = 1$ (lattice units); G_b is a parameter that tunes water-water molecular interactions. Through Taylor expansion, the nonideal fluid with the equation of state is recovered as $p = c_s^2\rho + \frac{c_s^2 G_b}{2}\psi^2$, with c_s as sound speed velocity. To avoid phase transition, parameter G_b should be tuned above a critical value $G_{b,c}$ ($G_{b,c} = -4$ in this case, as shown in Appendix D). Besides water-water interactions, water-solid interactions can be fulfilled by assuming an exponentially decaying external force with distance from the wall surface, the force being described as [93,94]

$$\mathbf{F}_w(\mathbf{x},t) = -G_w\rho(\mathbf{x})e^{-|\mathbf{x}-\mathbf{x}_w|/\lambda}, \qquad (11)$$

where $\mathbf{x}_w$ is a vector perpendicular to the wall surface; λ is the typical length scale controlling water-solid interactions, 0.3 nm [39,50]; and G_w is a parameter that tunes water-solid molecular interactions. The dynamic effects of the two forces are imposed onto the LB frame by adding velocity increment $\delta\mathbf{u} = \tau(\mathbf{F}_b+\mathbf{F}_w)/\rho$ to macroscopic velocity $\mathbf{u}$ [Eq. (5)] [95]. Then, in the next propagation, the newly calculated density-distribution function is updated correspondingly. Meanwhile, actual fluid velocity is redefined by adding velocity increment $\delta\mathbf{u} = \Delta t(\mathbf{F}_b+\mathbf{F}_w)/2\rho$ to macroscopic velocity $\mathbf{u}$ [Eq. (5)].

Considering the distinct one-molecular-diameter layering characteristics of the density profile and its symmetry with respect to the center of the nanochannel, the coarse grids with one-density-layer size in the LB frame can be implemented to represent local density. Then the grid numbers in the radial direction can be calculated by $N_y = (d-2\delta)/\sigma$. To connect the density between lattice Boltzmann (LB) space and physical space, we let the fluid density of the near-wall grid in the LBM match the density of the first layer calculated by Eq. (4). Then the relationship between the contact angle and tuning parameters (G_b and G_w) can be obtained. For all the simulations in this work, we constrained $G_b = -1.5$ and changed G_w to meet different wettability, and the simulation result is shown in Fig. 3(a). Hence, under a certain contact angle of nanochannel, the tuning parameter G_w can be calculated through interpolation. Following the parameter tuning strategy in Fig. 3(a), the density profiles under different contact angles are shown in Fig. 3(b). After the force terms are included, the density in the channel is no longer a constant value. In the proximity of the wall surface, the liquid water density can be increased or decreased compared with the density in the bulk. The existence of the density inhomogeneity does not need to be postulated *a priori*, but it emerges naturally when the molecular interactions are exerted. An inhomogeneous density profile was found to cause the nonparabolic shape of the velocity profile in the near-wall region. If we extrapolate the velocity from the velocity profile to the interface position, a positive or negative nonzero velocity exists, as shown in Fig. 3(c). In particular, apparent slip length $l_{s,a}$ is a negative value in a strong hydrophilic situation and is positive in a strong hydrophobic situation, inversely proportional to the density of the near-wall region [47,96]. It should be noted that, generally, viscosity is a measure of the fluidity. In LBM simulation, the viscosity and density in LBM have same effects on the flow velocity when we use external force to drive molecules [94]. In the following sections, a constant bulk viscosity at corresponding temperature was adopted to fit the MD simulation data from different literature. Under different radial grid numbers, the nearly consistent density profile in the near-wall region suggests that the LBM, with force terms included and one-diameter resolution, is stable and reasonable for simulating water confined flow in a wide range of channel sizes, as shown in Fig. 3(d).

True slip length can be modeled explicitly by using a combination of bounceback and specular reflection boundary in Eq. (6) while describing the apparent slip length implicitly by exerting the coupling molecular interactions between water-water [Eq. (10)] and water-solid [Eq. (11)]. Then both of the two mechanisms have been properly taken into account in LBM in a simulation of confined-water-flow behavior. The following section shows how water flow through infinite-length (47 cases) and finite-length nanochannels (50 cases) was investigated for a direct comparison with flow under the same conditions as those from MD simulations and experiments.

B. Validation in infinite-length nanochannels

The flow-enhancement factor, defined as the ratio of measured flow rates to those predicted by no-slip Poiseuille flow, is a critical performance parameter that characterizes the degree of deviation from traditional macroscale inside nanochannels [42]. In the case of confined water flow in infinite-length nanochannels, widely scattered flow-enhancement factor ε, ranging from 0.1 to 500 000, has been reported in recent years [9,18,19]. *Infinite-length nanochannel* means that the length of the tube in the experiments is long enough or that boundary conditions in MD simulations are periodic [Fig. 4(a)]. For example, Holt *et al.* [35] experimentally measured the flow rate of water flow through 1.3- to 2-nm-diameter and 6-μm-thick CNTs, and they found that enhancements were as high as 8 400. However, measurements of Gruener *et al.* [97] suggest that water flow is hindered in hydrophilic silica having a 6-nm pore diameter and that enhancement is smaller than 1. Anomalous flow behaviors arise from the significantly different relative interactions between water-water and water-solid, which both depend strongly on wall-surface wettability [Eq. (8), Figs. 3(b) and 3(c), and Fig. 4(b)]. In tubes having characteristic sizes of more than 1.6 nm, we noted that deviations from the classical no-slip description resulting from the presence of strong molecular interactions could be taken into account properly within the framework of Navier-Stokes constitutive equations [98].

In exerting different relative interactions between water-water and water-solid, 47 cases, composed of 23 cases from experiments [35,42,99–102] and 24 cases from MD simulations [98,103–107] in the literature, were simulated and

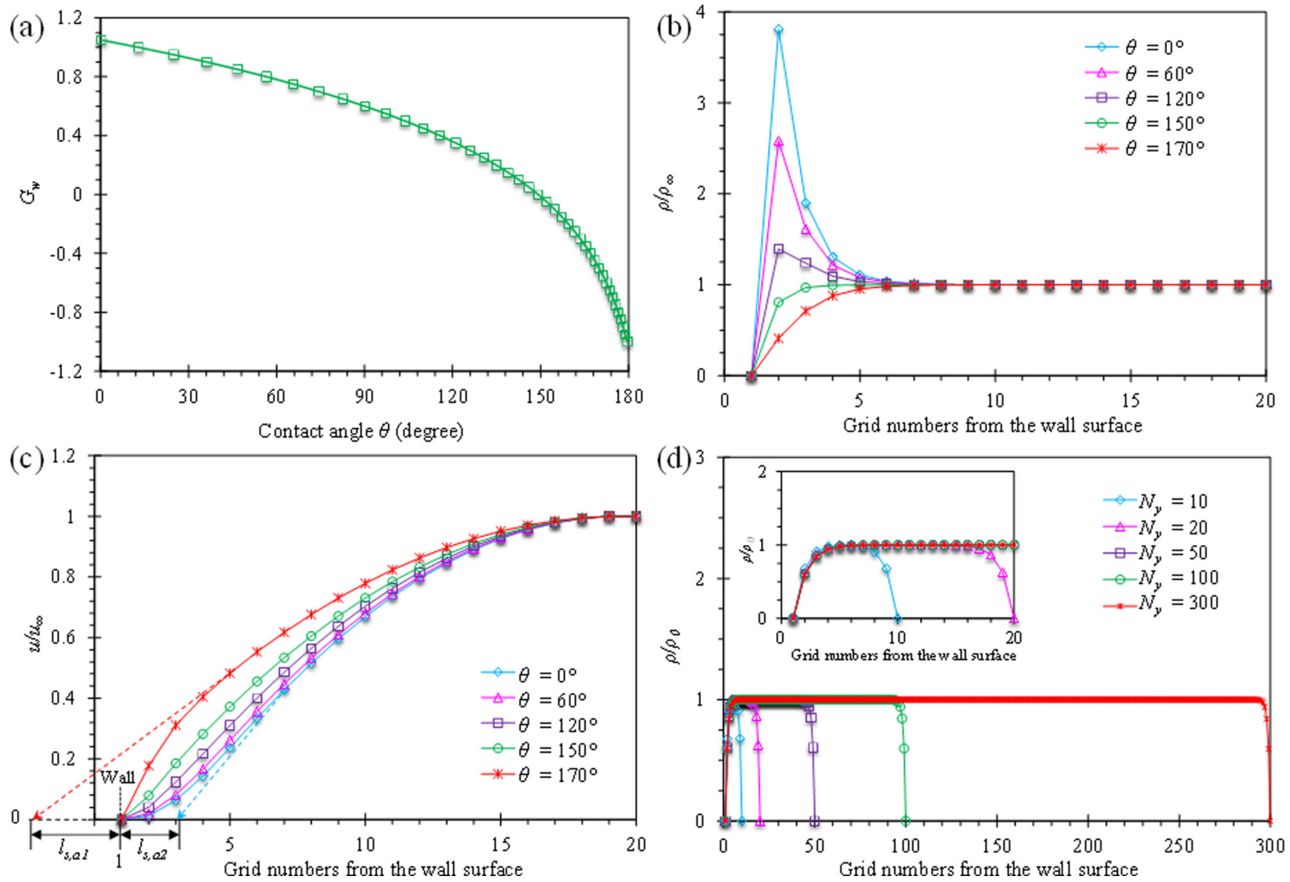

FIG. 3. (a) Relationship between the tuning parameters (G_b and G_w) and wettability. (b) Density profiles under different contact angles in proximity of the wall surface. For the hydrophilic wall surface (e.g., $\theta = 0^\circ$), the water density is increased in the near-wall region; for the hydrophobic wall surface (e.g., $\theta = 170^\circ$), the density is decreased in the near-wall region. (c) Velocity profiles under different contact angles in proximity of the wall surface. The colorful solid lines are the velocity profiles. The red and blue dashed arrows are the extrapolated velocity for $\theta = 0^\circ$ and $\theta = 170^\circ$, respectively. The corresponding apparent slip lengths are $l_{s,a1}$ and $l_{s,a2}$. As shown, $l_{s,a1}$ is a positive slip length, whereas $l_{s,a2}$ is a negative slip length. The wall interface is located in the first grid. Notably, to decouple the contribution of apparent slip and true slip, only the apparent slip after incorporation of Eqs. (10) and (12) is tested here, and the true slip length from Eq. (7) is zero. (d) Density profiles in different radial grid numbers ($\theta = 160^\circ$). At a fixed grid resolution (one molecular diameter), the water confined flow in different channel sizes with the range of 2.72 nm ($N_y = 10$) to 83.92 nm ($N_y = 300$) is simulated.

reproduced under matching conditions using the proposed LBM. Figure 4(c) shows the comparison results of enhancement factor ε, and detailed parameters are shown in Appendix F. Note that enhancement factor ε from experiments (3 data points) [99] or MD (1 data point) [107] for the BNNTs cannot be reproduced by our proposed LBM because the true slip length $l_{s,t}$ was not determined completely by wetting properties. This is because BNNTs have greater corrugation of the energy landscape arising from specific electronic structure effects, which is not related to its wetting properties [51].

In addition to the enhancement factor, density-layering effects, as well as velocity profiles in nanochannels, have been well predicted simultaneously (Figs. 5, 6). Specifically, only the first peak density value was used as the input parameter into the LB fame, although subsequent density profiles (subsequent layers) were characterized well using proposed force terms [Eqs. (10) and (11)]. The density upon approaching the wall surface is larger than that in the bulk region under hydrophilic conditions, whereas its value can be smaller than the density in the bulk region under superhydrophobic conditions. In the hydrophilic situations, the velocity profiles are nearly parabolic shape except the near-wall region, whereas the parabolic shape changes into a plug shape in the hydrophobic situations. Therefore, the interaction of the fluid and inner pore wall can dramatically affect water flow in nanochannels. There are experimental data that shows water flow in nanochannels could deviate from Hagan-Poiseuille equation both negatively (lower than HP predictions) and positively (up to six orders of magnitude higher than HP predictions). The discrepancy respectively lies in water negative and positive slippage at the pore inner wall. We tested systems with various material types and dimensions of nanochannels to reconcile the longstanding debate that when and why the flow rate of confined water is reduced or enhanced, compared with that obtained by the no-slip HP equation. It should be noted that, strictly, the data collected in Figs. 5 and 6 need to come from the same sources. However, most velocity profiles of the cases in Fig. 2 were not given in the original literature, and the enhancement factor is a much more popular parameter to characterize the confined flow dynamic performance. The

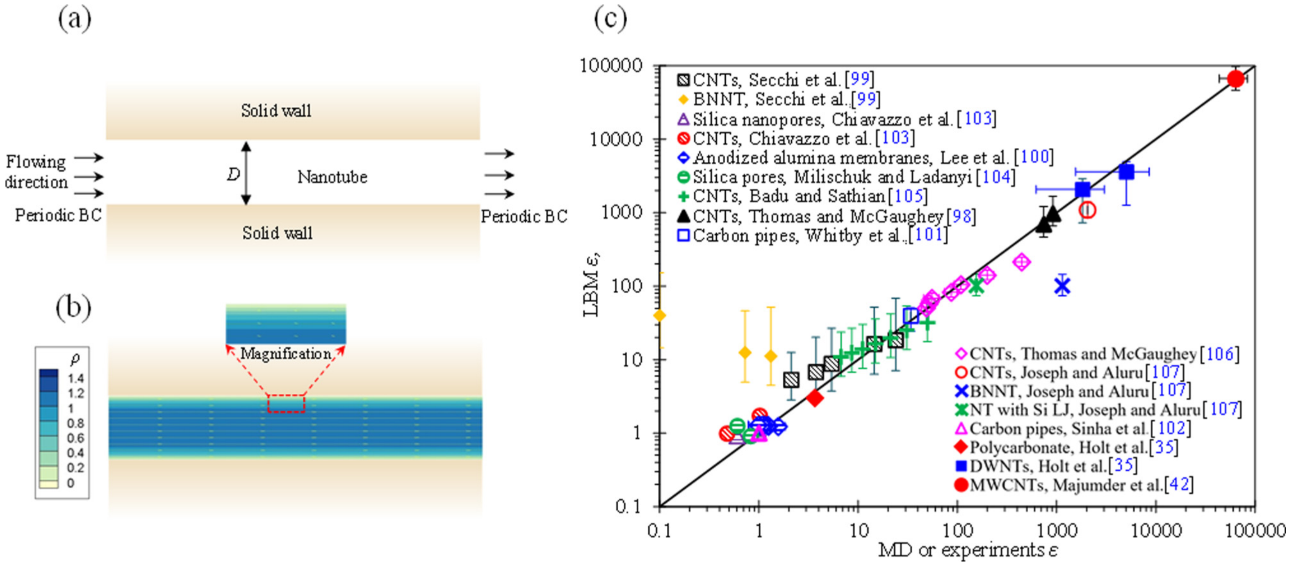

FIG. 4. Confined water flow in an infinite-length nanochannel. (a) Schematic of simulated domain with periodic boundary conditions (BC) on both sides. (b) Example of LBM simulation results for confined water flow in an infinite-length nanochannel ($\theta = 160^\circ$). Fluid density (lattice unit) near the wall surface is decreased in the hydrophobic tube by molecular interactions. (c) Comparison of experiments or MD simulation-enhancement factor ε from literature and simulation-enhancement factor ε by our proposed LBM under identical conditions (infinite-length nanochannel). Comparison includes 47 cases from literature, in which 23 cases are experiments [35,42,99–102] and 24 cases are MD simulations [98,103–107]. The comparison shows most cases from different research can be recovered well. The black diagonal line guides the reader's eye to the comparison. Error bars in enhancement factor ε originate from uncertainties in determination of contact angles or tube size.

good fitting results in Fig. 6 indicate that, as long as the wettability is a known parameter, the density fitting from one set can be used to get the enhancement factor from a different set without using the first set of data.

C. Validation in finite-length nanochannels

In the problem of water flow through finite-length nanochannels, in addition to the discussed complexities of flow behavior within the channel, entrance and exit effects are of particular importance [Fig. 7(a)]. A *finite-length nanochannel* is a short tube with a length about ten times the tube diameter that is connected to two water baths at the inlet and outlet [108]. In the case of hydrophilic nanochannels, in which a negative effective slip length occurs, entrance and exit resistance becomes less significant because resistance within the channel is relatively high [108]. However, in tubes such as CNTs and aquaporin, their smooth surfaces and hydrophobicity provide surprisingly low frictional loss inside the tubes [109]. When water molecules enter or exit these nanochannels, streamlines curve sharply from the large reservoirs into (or out of) the relatively smaller tubes [Fig. 7(b)], leading to a plug flow-velocity profile along the inner tubes and a negligible inside flow resistance, as compared with entrance and exit resistance [110]. In particular, the hydrodynamic entrance and exit effect involving additional viscous dissipation is expected to be a dominant resistance contributor in systems of short length and/or systems with strong hydrophobicity (low friction) at their wall surface [108,109], challenging the system with a requirement of high flow rate.

The contribution of the hydrodynamic entrance and exit effect is, however, well understood and has been characterized recently [108]. Furthermore, several methods are known to reduce an end effect in maintaining a fast mass-transport rate [111,112]. Here, we used our proposed LBM to simulate confined water flow finite systems to show the importance of pressure loss at the ends. A total of 50 cases were simulated and reproduced under conditions identical to those from MD simulations [25,36,37,108,113] in the literature. Figure 7(c) shows comparison results between enhancement factor ε; detailed parameters are shown in Appendix F. We found good agreement in most cases between MD simulations and those obtained from LBM prediction. However, CNT data (6 data points) by NAMD with external force of 20 MPa from Walther *et al.* [37] do not fit well in this work, nor do they in studies by Popadić *et al.* [114], Ritos *et al.* [36], or Suk and Aluru [108]. In addition, we found that the end effects greatly reduce flow capacity in short hydrophobic tubes. Note that our LBM simulations required only 1 h for a micrometer-scale-length case, when an i5, eighth-generation computer was used, whereas more time is required for a supercomputer with thousands of processors to complete MD simulations under the same scale [36,37].

IV. DISCUSSIONS

Although in principle, MD simulation is the most popular and credible tool for describing fluid dynamic behavior at the microscopic scale [9], its handling of time and space scales for liquid (water) is typically on the order of several hundreds of nanoseconds and several tens of nanometers, respectively [36,37]. LBM, a minimal version of the kinetic equation, is a good candidate for solving this problem [115] because it works between the atomistic and continuum scale

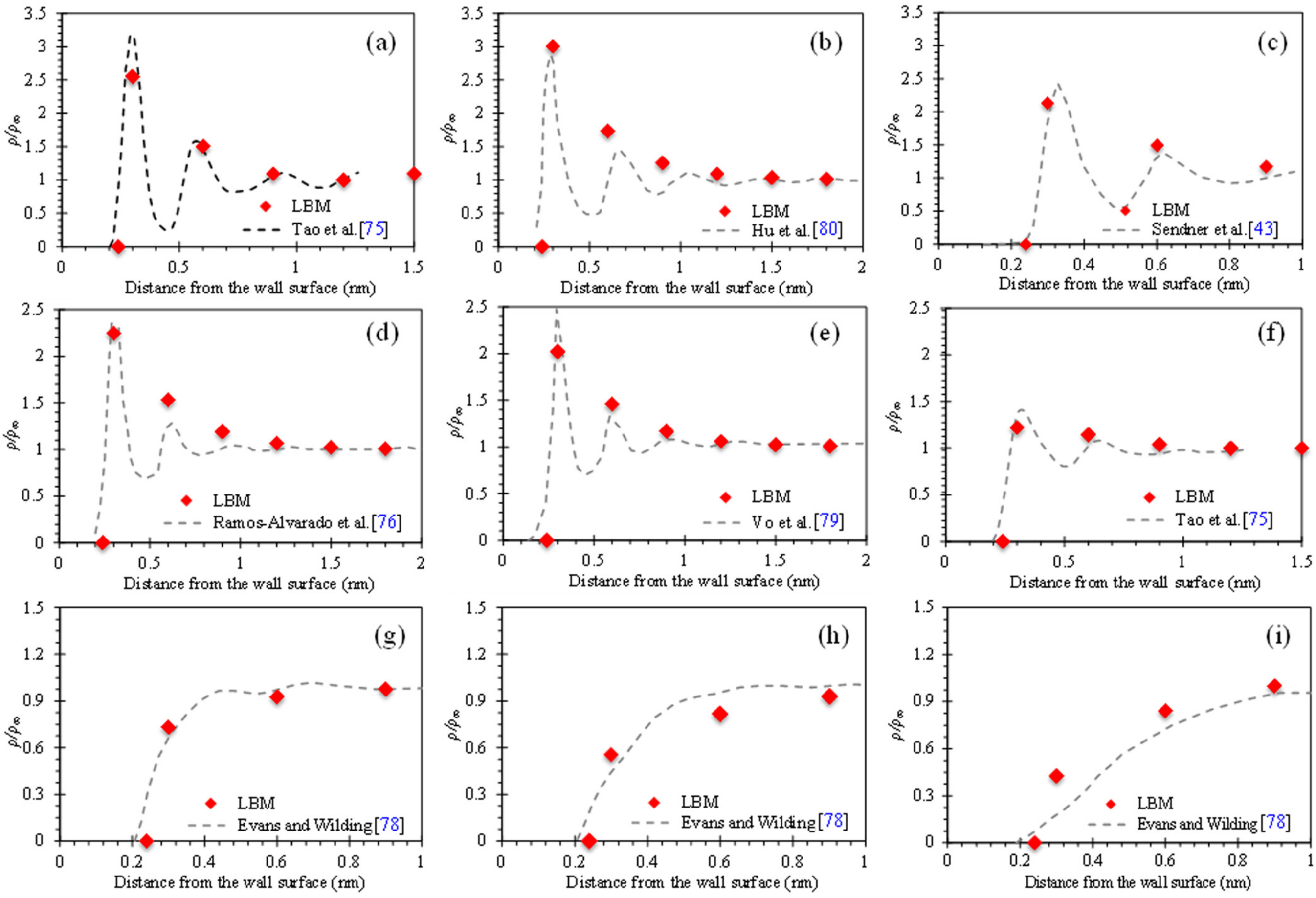

FIG. 5. Comparison of the density profiles from MD simulations (gray dashed line) in the literature and the one by the proposed LBM (red dots) under the same conditions. The nine cases cover the wettability from hydrophilic to superhydrophobic channels with different dimensions and materials [43,75–77,78–80], and all the comparisons show the proposed mesoscopic LBM can reproduce the continuous density profile in a molecularly coarse-grained way. The contact angle, channel size, and LBM grids of the simulated cases are (a) $\theta = 13^\circ$, $d = 2.5$ nm, $N_y = 9$ [75]; (b) $\theta = 30^\circ$, $d = 10$ nm, $N_y = 36$ [80]; (c) $\theta = 52^\circ$, $d = 4$ nm, $N_y = 15$ [43]; (d) $\theta = 71^\circ$, $d = 5$ nm, $N_y = 18$ [76]; (e) $\theta = 86.1^\circ$, $d = 7$ nm, $N_y = 25$ [79]; (f) $\theta = 120^\circ$, $d = 2.5$ nm, $N_y = 9$ [75]; (g) $\theta = 154^\circ$, $d = 10$ nm, $N_y = 36$ [78]; (h) $\theta = 163^\circ$, $d = 10$ nm, $N_y = 36$ [78]; (i) $\theta = 178^\circ$, $d = 10$ nm, $N_y = 36$ [78].

and does not take the atomistic details into account. In this work, one molecular-sized, coarse-grained method was implemented on LBM, and the disadvantage is that could only reflect averaged effects of molecular interactions and not fully reproduce the density or velocity profile in proximity of the wall surface below one lattice grid resolution. MD simulation is a powerful tool in modelling nanoscale water flow process in small systems such as a single nanochannel. However, for large nanosystems such as a network of nanochannels, MD is limited due to the need of exorbitant computational resources. Our proposed LBM could be a computationally efficient method to study water flow in complex nanosystems such as nanoporous material if the macroscopic behavior is of interest rather than the details of radial density variation in individual pores. In LBM, we based our coarse-grained model on direct data mapping from MD simulations or experiments to allow a direct comparison of the influence of water-solid interactions in the LB frame on the density profile, velocity profile, and enhancement factors [116,117]. Moreover, tuning parameters (G_w and G_b) in the model have no less physical meaning than their atomistic counterparts in MD simulations (particle-wall interaction and inverse temperature), notwithstanding an intrinsically mesoscopic characteristic [115]. Although the treatment of force term inspired from Shan-Chen scheme in this work has the advantages of simplicity and clear physical reflection of fluid flow, it still has its weakness in accuracy because the effects of the interaction force are reflected in the first-order moment of the equilibrium distribution function [116,117], and researchers can develop a more accurate force treatment in the future.

Wettability of the nanochannel surface was used as a fundamental property for characterizing true and apparent slip length in the LBM explicitly and implicitly, respectively, indicating that, besides nearly frictionless walls [101,118] and surface nanobubbles [59], the strong hydrophobic channel surface could also enhance water flow rates in confinement dramatically [51,66,119]. Note that great attention should be paid to accurate determination of the contact angle for a strong hydrophobic channel surface, as slip length is a highly sensitive quantity [66]. In addition, because the input parameters of the LBM are from MD simulations for ideal atomically smooth surfaces, the model cannot be applied to

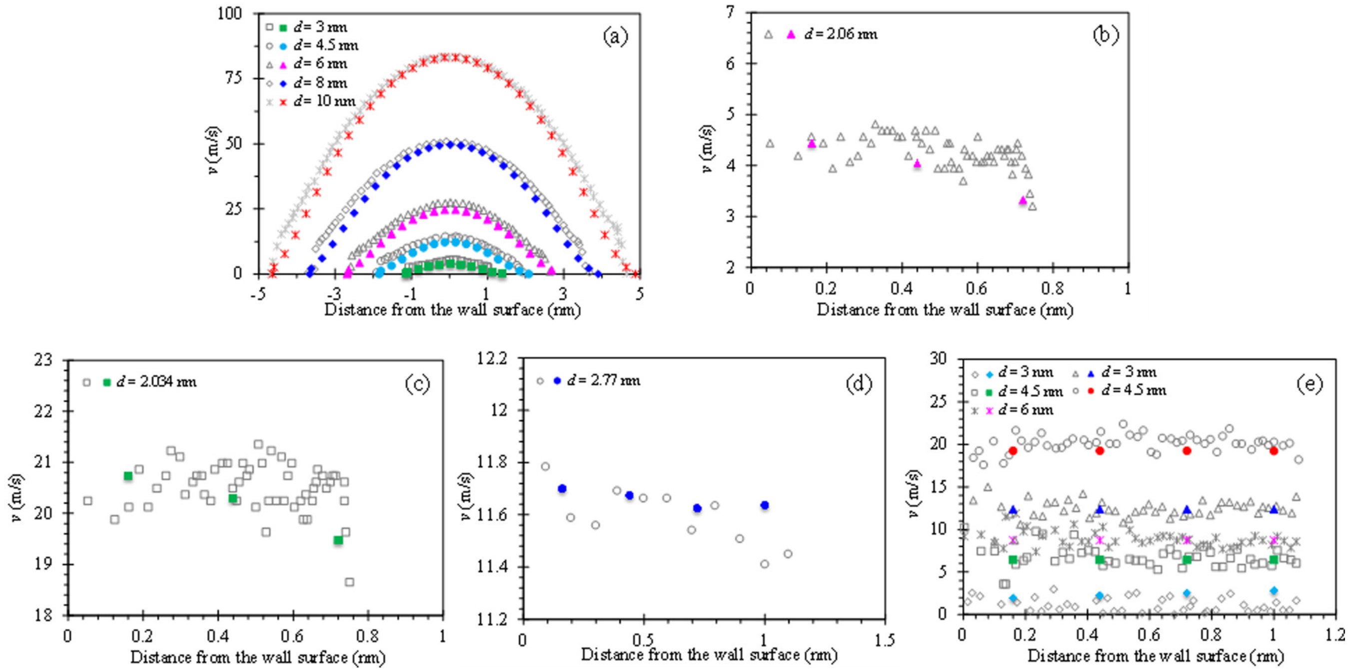

FIG. 6. Comparison of the velocity profiles from MD simulations (gray hollow dots) in the literature and the one by the proposed LBM (colored dots) under the same conditions. The five cases cover the wettability from hydrophilic to hydrophobic channels with different dimensions and materials [25,81,84,108], and all the comparisons show the proposed mesoscopic LBM can reproduce the velocity profile in a molecularly coarse-grained way. The external forces in these cases are shown in a form of MD in the original literature. To avoid the unit conversion and achieve the fitting, we assume the external force is 1 MPa/nm in LBM simulations, and the simulated LBM velocity profiles are scaled by the center velocity of MD to obtain the final values. The contact angles of the simulated cases are (a) $\theta = 43^\circ$ [81]; (b) $\theta = 105.5^\circ$ [25]; (c) $\theta = 130.5^\circ$ [25]; (d) $\theta = 150^\circ$ [84]; (e) $\theta = 161.5^\circ$ [108].

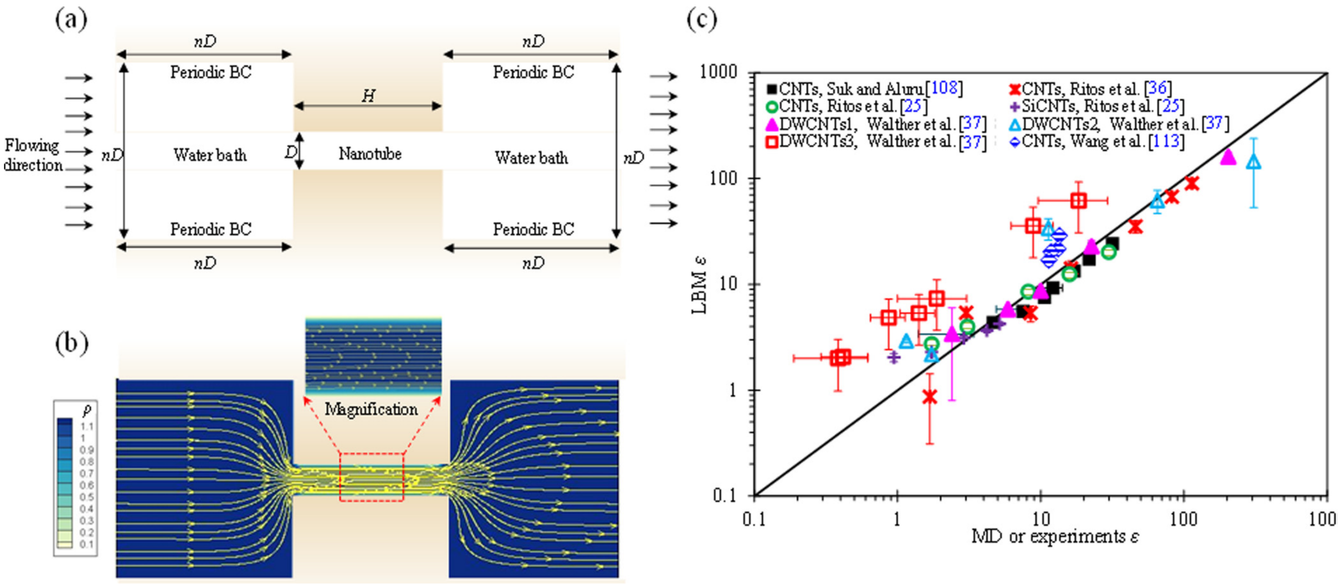

FIG. 7. Confined water flow in a nanochannel with end effects (finite-length nanochannel). (a) Schematic of simulated domain with two water baths connected on both ends. Rationalization of value n is calibrated in Appendix E. (b) Example of LBM simulation results for confined water flow with ends ($\theta = 160^\circ$). Bending of streamlines (yellow arrowed lines) at entrance and exit induces significant additional flow resistance, compared with flow through infinite nanochannels. Density is lattice unit. (c) Comparison of experiments or MD simulation enhancement factor ε from literature and simulation enhancement factor ε from our proposed LBM under identical conditions (finite-length nanochannel). Comparisons, including 50 cases from MD simulations [25,36,37,108,113]. Comparison shows most cases from different studies can be matched well. The black diagonal line guides the reader's eye to the comparison. Error bars of enhancement factor ε originate from uncertainties in determination of contact angles or external force.

modeling a nanosystem having dissolved gas or a contaminant that possibly occurred in practical conditions [62,64].

We have tried to show the outstanding advantages of the proposed LBM in its fruitful applications for complex geometrical boundaries in simulation of confined flow with entrance and exit effect. Moreover, the simulations can be extended to 3D nanochannels having different cross-section shapes [120,121], tortuous channels with rough surfaces [115], and experimentally accessible scales—nanoporous media (CNTs membrane [4,37], aquaporins [111], shale matrix [5,8], etc.)—with easily available computational resources. For the water flow in complex nanoporous media, the current treatment of boundary condition has the limitation in determination of specular reflection directions for the irregular surface, while the combined bounce-back and full diffusive boundary condition [56] is more powerful in handling a complex geometry, which should be considered in the future work. The adaptive mesh-refinement scheme using a nonuniform mesh strategy can be developed in the future to provide the one-molecular-diameter resolution in the near-wall region and rougher grids in the bulk [122], since the water-solid interactions causing a slip phenomenon are generally located within a few molecular layers near the boundary surface [68,70]. This strategy will further boost the proposed LBM at a lower computational cost in solving much larger systems in time and space, yielding molecular-scale, accurate results such as in MD simulations.

V. CONCLUDING REMARKS

In summary, we developed a mesoscopic LBM framework using embedded nanophysics for water flow in nanoconfined systems, such as nanochannels. We have made two major modifications to the conventional LBM to model the effects of wettability on water flow in nanochannels: (i) modified the fully bounce back boundary to mixed boundary to capture the true slip length; (ii) included water-water force and water-solid force to capture the apparent slip. The fluctuated density distribution and nonparabolic velocity profile in the proximity of wall surfaces can be well captured, and simulation results of the proposed method are in good agreement with most of the 47 different cases of water flow through infinite-length tubes and 50 different cases through finite-length tubes reported in the literature. We quantitatively explained the discrepancies over an enhancement or reduction in flow capacity in MD simulations and experiments, as well as the hindrance of the entrance and exit effect on flow behaviors. The proposed framework predicts water flow in nanochannels with the accuracy of MD simulations but computationally more efficient, opening up a new avenue for modeling confined water flow in much larger and complex nanosystems.

ACKNOWLEDGMENTS

We thank Dr. Mohamed Ibrahim Shaat (New Mexico State University) and Dr. Zhenhua Chai of (Huazhong University of Science and Technology) for helpful discussions and MinXia He (China University of Petroleum) for help in simulations. This work is supported by the National Natural Science Foundation Projects of China (Grants No. 50974128, No. 51504269, and No. 51490654); the National Science and Technology Major Projects of China (Grants No. 2016ZX05042, No. 2017ZX05009003, and No. 2017ZX05039005); the Science Foundation of China University of Petroleum, Beijing (Grants No. 2462018YJRC033 and No. C201605); NanoGeosciences lab; and the Mudrock Systems Research Laboratory at the Bureau of Economic Geology. T.Z. also acknowledges the China Scholarship Council (CSC) for its financial support of his living expenses at The University of Texas at Austin as a visiting Ph.D. student.

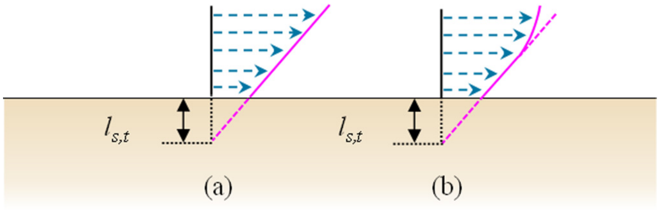

FIG. 8. Sketch of the linear (a) (Couette flow) and (b) nonlinear velocity distribution (channel flow) with Navier linear slip assumption in the boundary [57].

APPENDIX A: VALUE OF RELAXATION TIME τ

The linear velocity gradient assumption for the first two layer-grids is used to model the flow with the nonlinear velocity gradient (channel flow) [123], as shown in Fig. 8. This assumption results in an additional error term $l_{s,\text{error}}$, associated with the grid numbers and the relaxation time [57]. If the grid is fine enough or the relaxation time equals 1.11, the error term can be avoided completely. Thus, τ is set at 1.11 for all the simulations in this work

$$l_{s,\text{error}} = \left(\frac{1}{4} - \frac{2}{3}(\tau - 0.5)^2\right)\frac{1}{N_y}. \tag{A1}$$

APPENDIX B: PARAMETER AND UNIT CONVERSION

The three basic quantities—length, time, and mass—are represented by diameter, viscosity, and density, respectively, the quantities of which are known in both physical space and lattice space, as shown in Table I. Then, all other unknown physical or lattice quantities (the number of lattice grids in flow directions, the true slip length, external force, velocity, etc.) can be derived by the three scale factors [124]. For example, the velocity scale factor can be calculated by $u_r = \upsilon_r / L_r$.

TABLE I. The basic parameters for unit conversion.

Parameters	Physical symbol	Lattice symbol	Scale factor
Diameter, m	D	N_y	$L_r = D/N_y$
Viscosity, m^2/s	υ	υ_e	$\upsilon_r = \upsilon/\upsilon_e$
Density, kg/m^3	ρ_p	ρ	$\rho_r = \rho_p/\rho$

TABLE II. A summary of various parameters used to reproduce Figs. 2(b), 9, and 10.

Investigators	Channel material	Temperature, K	Channel diameter, nm	Contact angle, °	δ_1, nm	δ_2, nm	ρ_1, g /cm^3
Tao *et al.* [75]	CNTs	300	2.50	109.61	0.33	0.31	1.58
				119.94	0.34	0.33	1.41
				131.50	0.35	0.33	1.11
Neek-Amal *et al.* [74]	Graphene	298	1.80	hydrophobic	0.27 ± 0.02	0.3 ± 0.02	2.57
Ramos-Alvarado *et al.* [76]	Silica	300	5.00	71.00	–	0.42	2.34
Vo *et al.* [77]	Cu	300	7.00	86.10	0.27	0.33	2.45
	Cu/Gra			92.70	0.31	0.27	2.15
Evans and Wilding[a] [78]	–		2	26.00	0.29	0.29	3.22
		fixed temperature		88.00	0.29	0.29	2.13
				117.50	0.30	0.30	1.55
				154.00	–	–	0.70
				163.00	–	–	0.45
				178.00	–	–	0.19
Vo *et al.* [79]	Cu	300	4.00	86.40	0.22	0.23	2.30
Walther *et al.* [37]	CNTs	–	2.03	95.00	0.30	0.32	2.35
Bonthuis and Netz [128]	$C_{20}H_{41}OH$	–	>3	hydrophilic	0.19	0.33	2.29
	$C_{20}H_{42}$			hydrophobic	0.35	0.31	1.56
Hu *et al.*[c] [80]	Pt		0.27	30.00	0.27	0.39	3.06
		–		60.00	0.27	0.39	2.68
				90.00	0.27	0.39	2.13
				120.00	0.27	0.39	1.72
				150.00	0.27	0.39	1.34
Botan *et al.* [81]	Clay	300	4.50	43.00	0.31	0.32	3.34
Sendner *et al.*[a] [43]	–		4.00	87.42[b]	0.33	0.31	1.96
		300		143.64[b]	0.39	0.31	1.01
				160.03[b]	–	–	0.53
Alexiadis *et al.* [82]	CNTs	–	3.52	104.50	–	0.34	1.87
				109.47	–	0.34	1.66
Chen [83]	–	–	–	0.00	0.31	–	3.90
Thomas and McGaughey [84]	CNTs	298	6.90	129.00[b]	0.30	0.41	1.15
Xiang *et al.*[c] [85]	Solid Ar		6.94	30.00	0.39	0.29	2.85
		–		60.00	0.38	0.34	2.29
				90.00	0.39	0.30	2.01
				120.00	0.40	0.34	1.77
				150.00	0.41	0.33	1.13
Priezjev *et al.* [129]	–	$k_BT/\varepsilon = 1.1$[d]	20.15σ	162.40[b]	0.27	0.31	1.69
Walther *et al.* [86]	CNTs	–	2.5	86.00	0.32	0.32	2.45
Werder *et al.* [87]	CNTs	300	–	95.30	0.32	0.29	2.66
Walther *et al.* [88]	CNTs	300	1.52	112.57[b]	0.32	0.32	1.94
Barrat and Bocquet [47]	–	$k_BT/\varepsilon = 1$[d]	9.00	150.00	0.54	0.45	0.97
Allen *et al.* [130]	ACh	300	1.12	hydrophilic	–	0.24	4.62
	Potassium			hydrophobic	–	0.27	2.96

[a] The density curve shows no density peak in the superhydrophobic nanochannel, so δ_1 and δ_2 are not used in the statistics, whereas the density value of ρ_1 is obtained by the assumption that δ_1 is 0.28 nm.

[b] The contact angle is not explicitly shown in the literature, and it is recalculated in this work by using the method introduced in Werder *et al.* [87].

[c] The simulated fluid is Ar, so the data δ_1 and δ_1 are not adopted to reproduce Figs. 9 and 10.

[d] A constant reduced temperature, where k_B is Boltzmann's constant and ε is interaction energy.

APPENDIX C: IDENTIFYING SEVERAL DISTANCES ON THE DENSITY CURVE

1. Stand-off distance

The stand-off distance δ is defined as the distance between the solid surface and the position of the first density peak. It should be excluded in the modeling of the water flow because no mass appears in this region [125]. For Lennard-Jones (LJ) fluid, the mean-field potential between the wall surface and the water, obtained by integrating the LJ potential, rises sharply as it approaches the wall surface, leading to a maximum position that is energetically accessible to the water [126]. Then, the stand-off distance can be derived analytically as follows

TABLE III. A summary of various parameters used to reproduce Fig. 4.

Investigators	Channel materials	Method	Channel diameter, nm	Channel length, nm	Contact angle[b], °	MD or exper ε	LBM ε	LBM ε error (+)[c]	LBM ε error (-)[c]
Secchi *et al.* [99]	CNTs	Exper.	30±2	450 ∼ 1000	155 ± 6	23.84 ± 3.5	18.44	50.01	11.38
			34±2		155 ± 6	14.53 ± 1.35	16.37	35.06	10.04
			66±2		155 ± 6	5.40	8.79	17.90	5.08
			76±6		155 ± 6	3.75	6.81	13.33	3.42
			100±6		155 ± 6	2.11	5.31	7.19	2.50
Secchi *et al.* [99]	BNNTs[a]	Exper.	14.00	600 ∼ 1300	–	0.10	–	–	–
			46.00		–	0.73	–	–	–
			52.00		–	1.32	–	–	–
Chiavazzo *et al.* [103]	Silica nanopores	MD	7.58	∞	60 ± 5	0.61	0.93	0.01	0.01
			2.54		60 ± 5	0.97	1.16	0.06	0.05
Chiavazzo *et al.* [103]	CNTs with Fe_3O_4 nanoparticles	MD	65.00	∞	55 ± 5	0.48	0.99	0.00	0.00
			1.65		55 ± 5	1.02	1.72	0.12	0.10
Lee *et al.* [100]	Anodized alumina membranes	Exper.	47±2	250000	12 ± 2	1.57 ± 0.28	1.23	0.01	0.01
			56±6		12 ± 2	1.25 ± 0.34	1.24	0.01	0.01
			60±5		12 ± 2	1.23 ± 0.28	1.27	0.01	0.01
			70±5		12 ± 2	1.14 ± 0.23	1.27	0.01	0.01
			69±6		12 ± 2	1.14 ± 0.25	1.27	0.01	0.01
			86±8		12 ± 2	1.03 ± 0.24	1.27	0.01	0.01
			82±10		12 ± 2	1.08 ± 0.29	1.28	0.01	0.01
			96±8		12 ± 2	0.99 ± 0.21	1.28	0.01	0.01
Milischuk and Ladanyi, [104]	Silica pores	MD	2.00	∞	45 ± 5	0.61	1.25	0.06	0.05
			4.00		45 ± 5	0.82	0.91	0.02	0.01
Babu and Sathian [105]	CNTs	MD	1.62		132 ± 8	49.81	31.92	34.88	14.43
			1.90	∞	132 ± 8	30.80	25.26	28.33	11.53
			2.17		132 ± 8	21.21	19.63	22.34	8.98
			2.44		132 ± 8	14.91	16.62	19.15	7.63
			2.71		132 ± 8	11.08	13.98	16.22	6.41
			2.98		132 ± 8	8.63	12.38	14.41	5.66
			3.25		132 ± 8	6.73	10.88	12.69	4.95
Thomas and McGaughey [98]	CNTs	MD	1.39	75	157.25 ± 2.5	916.78	976.57	696.29	317.14
			1.66	150	157.25 ± 2.5	740.70	696.15	513.85	230.77
Whitby *et al.* [101]	Carbon pipes	Exper.	44±3	78000±2000	161 ± 1	34.02	39.56	11.11	15.10
Thomas and McGaughey [106]	CNTs	MD	4.99	∞	150 ± 1	48.75 ± 5.4	50.68	8.74	7.12
			4.44		150 ± 1	52 ± 8.09	58.19	9.93	8.27
			3.88		150 ± 1	55.45 ± 9.89	68.30	11.72	9.68
			3.33		150 ± 1	86.82 ± 12.59	82.68	13.82	11.48
			2.77		150 ± 1	108.68 ± 16.19	104.72	17.24	14.36
			2.22		150 ± 1	199.71 ± 33.27	141.27	22.70	18.97
			1.66		150 ± 1	444.46 ± 63.85	214.50	33.12	27.81
Joseph and Aluru [107]	NT with Si LJ	MD	2.17	∞	147.5 ± 2.5	155.00	102.46	42.86	28.17
Joseph and Aluru [107]	BNNTs[a]	MD	2.17	∞	–	1142.00	–	–	–
Joseph and Aluru [107]	CNTs	MD	2.17	∞	161 ± 1	2052.00	1087.3	301.59	222.22
Sinha *et al.* [102]	Carbon pipes	Exper.	300	10000	44	1.00	1.00	0.00	0.00
Holt *et al.* [35]	DWCNTs	Exper.	1.30 ∼ 2.00	2000 ∼ 3000	163 ± 2	5049.62	3614.29	2475.71	1340
			1.30 ∼ 2.00		163 ± 2	1822.72	2070.18	1508.77	807.02
Holt *et al.* [35]	Polycarbonate	Exper.	15.00	6000	135 ± 2	3.67	3.01	0.51	0.39
Majumder *et al.* [42]	MWCNTs	Exper.	7.00	34000	175 ± 0.5	63746.99			

[a] The enhancement factor ε from exper. (experiment) or MD for boron nitride nanotubes (BNNTs) cannot be reproduced by our proposed LBM because the true slip length $l_{s,t}$ of BNNTs is not completely controlled by wetting properties.

[b] The contact angles that are not explicitly shown in the literature are from Wu *et al.* [51].

[c] The errors of enhancement factors ε originate from the uncertainties in determination of contact angles or channel size.

TABLE IV. A summary of various parameters used to reproduce Fig. 7.

Investigators	Channel materials	Method	Channel diameter, nm	Channel length, nm	Contact angle[b], °	External pressure, MPa/nm	MD or exper ε	LBM ε[c]
Suk and Aluru [108]	CNTs	NAMD	3.94	5.76	161.5 ± 1.5	$0.17 \sim 60$	4.66	4.37 ± 0.20
				10.68	161.5 ± 1.5	$0.17 \sim 60$	7.52	5.56 ± 0.17
				15.46	161.5 ± 1.5	$0.17 \sim 60$	10.59	7.54 ± 0.2
				20.28	161.5 ± 1.5	$0.17 \sim 60$	12.14 ± 2	9.29 ± 0.24
				30.85	161.5 ± 1.5	$0.17 \sim 60$	17.09	13.36 ± 0.30
				41.48	161.5 ± 1.5	$0.17 \sim 60$	21.71	17.34 ± 0.60
				61.56	161.5 ± 1.5	$0.17 \sim 60$	31.62	24.29 ± 0.88
Ritos *et al.* [36]	CNTs	Hybrid MD	2.034	2.41	155.5 ± 2.5	82.83	1.68	0.87 ± 0.56
				5.01	155.5 ± 2.5	39.94	3.01	5.39 ± 0.43
				12.09	155.5 ± 2.5	16.54	8.50	5.34 ± 0.92
				24.33	155.5 ± 2.5	8.22	16.27	14.14 ± 2.61
				48.95	155.5 ± 2.5	4.09	45.92	35.31 ± 4.57
				98.49	155.5 ± 2.5	2.03	82.32	67.09 ± 5.70
				146.22	155.5 ± 2.5	1.37	113.85	90.28 ± 9.26
Ritos *et al.* [25]	CNTs	MD	2.034	2.51	130.5	79.65	1.73	2.73
				5.02	130.5	39.86	3.07	3.99
				12.57	130.5	15.92	8.18	8.53
				25.49	130.5	7.85	15.85	12.46
				50.94	130.5	3.93	29.85	20.16
Ritos *et al.* [25]	BNNTs[a]	MD	2.072	2.56	–	78.19	0.53	–
				5.04	–	39.72	1.37	–
				12.61	–	15.86	3.87	–
				25.20	–	7.94	5.96	–
				50.35	–	3.97	8.18	–
Ritos *et al.* [25]	SiCNTs	MD	2.062	2.51	105.5	79.76	0.94	2.04
				5.09	105.5	39.32	1.73	2.29
				12.55	105.5	15.94	2.90	3.11
				25.46	105.5	7.86	4.22	3.65
				50.11	105.5	3.99	5.16	4.23
Walther *et al.* [37]	DWCNTs1	FASTTUBE	2.034	2.78	155 ± 5	7.19	2.40	3.40 ± 2.60
				5.73	155 ± 5	3.49	5.89	5.82 ± 0.23
				11.50	155 ± 5	1.74	10.00	8.69 ± 0.14
				29.10	155 ± 5	0.69	22.60	22.89 ± 2.90
				296.00	155 ± 5	0.068	204.00	160.53 ± 15.03
Walther *et al.* [37]	DWCNTs2	NAMD	2.034	1.35	155 ± 5	1.48	1.73	2.18 ± 0.12
				2.12	155 ± 5	0.94	1.15	2.92 ± 0.12
				48.60	155 ± 5	0.041	11.30	33.99 ± 7.86
				97.00	155 ± 5	0.0021	65.20	61.88 ± 14.55
				478.00	155 ± 5	0.00042	307.00	146.02 ± 92.92
Walther *et al.* [37]	DWCNTs3	NAMD	2.034	1.35	155 ± 5	14.81	0.42 ± 0.21	2.07 ± 0.02
				2.12	155 ± 5	9.43	0.38 ± 0.24	2.00 ± 1.02
				3.14	155 ± 5	6.37	0.87 ± 0.24	4.84 ± 2.42
				5.08	155 ± 5	3.94	1.04 ± 0.38	5.33 ± 2.67
				9.85	155 ± 5	2.03	1.88 ± 1.02	7.34 ± 3.67
				48.60	155 ± 5	0.41	8.85 ± 3.00	35.72 ± 17.86
				97.00	155 ± 5	0.21	18.40 ± 9.80	61.71 ± 30.88
Wang *et al.* [113]	CNTs	NAMD	1.63	3	85 ± 5	1.67	13.5	1.84 ± 2.18
				6	85 ± 5	0.83	13.2	2.11 ± 2.067
				9	85 ± 5	0.56	11.8	2.48 ± 1.99
				15	85 ± 5	0.33	11.4	2.78 ± 1.99

[a] The enhancement factor ε from exper. (experiment) or MD for BNNTs cannot be reproduced by our proposed LBM because the true slip length $l_{s,t}$ of BNNTs is not completely controlled by wetting properties.

[b] The contact angle is not explicitly shown in the literature, and it is recalculated in this work by using the method introduced in Werder *et al.* [87]. The contact of Wather *et al.* [37] is estimated by Eq. (9) with a slip length of 64 nm [114].

[c] The errors of enhancement factors ε originate from the uncertainties in the determination of contact angles or external pressure.

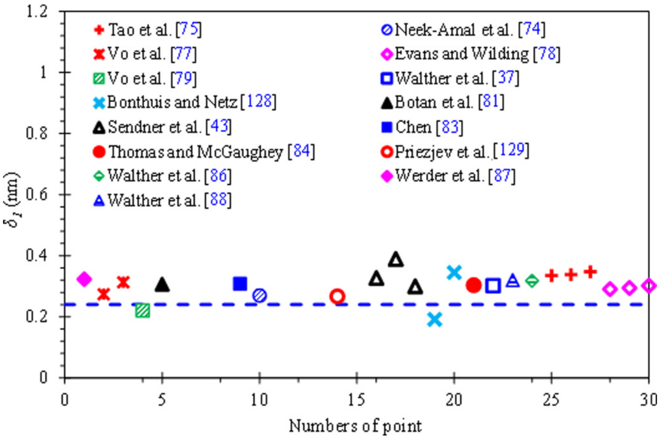

FIG. 9. Determination of the distance between the solid surface and the location of the first density peak δ_1. The data are from MD simulations in the literature, and the simulated wall surfaces are (1) flexible and rigid carbon nanotubes (CNTs) with various surface wettability (Tao *et al.* [75]); (2) flat walls with two graphene layers (Neek-Amal *et al.* [76]); (3) Cu and graphene-coated Cu surface wall (Vo *et al.* [77]); (4) Lennard-Jones hydrophobic substrate (Evans and Wilding [78]); (5) Au surface wall (Vo *et al.* [79]); (6) double-walled carbon nanotubes (DWCNTs) (Walther *et al.* [37]); (7) self-assembled monolayers consisting of single membranes of either $C_{20}H_{41}OH$ or $C_{20}H_4$ (Bonthuis and Netz [128]); (8) sodium-saturated Wyoming montmorillonite surface to represent clay (Botan *et al.* [81]); (9) hydrophobic hydrogen terminated diamond surface (Sendner *et al.* [43]); (10) Lennard-Jones substrate (Chen *et al.* [83]); (11) armchair CNTs (Thomas and McGaughey [84]); (12) two (111) planes with an face-centered cubic (FCC) lattice consisting of 12,288 molecules (11)(Priezjev *et al.* [129]); (13) zigzag CNTs (Walther *et al.* [86]); (14) CNTs (Werder *et al.* [87]); (15) CNTs (Walther *et al.* [88]). The blue dashed line with the value of 0.28 nm is drawn to guide the reader's eyes.

[127]:

$$\delta = (2/5)^{1/6}\sigma, \qquad \text{(C1)}$$

where σ is the molecular diameter, set at 0.28 nm for water [89]. Thus, the stand-off distance in this paper equals 0.24 nm, solely dependent on the molecular diameter [127].

2. The distance between the solid surface and the location of first density peak

The distance between the solid surface and the location of the first density peak δ_1 is a critical parameter to characterize the density structure. In the position of the first density peak, the mean-field interaction potential reaches a minimum, and the position can be obtained by setting the derivative of the mean-field interaction potential at zero [127], roughly equal to the diameter of the molecule. Further, statistical data extracted from the literature also support this conclusion well, as shown in Fig. 9.

3. The distance between the location of the first density peak and the second density peak

The density profile is a distance-related oscillatory function having roughly a molecular diameter period, and the period is within the range of a few molecular diameters near the wall [50]. The location of the first density peak and the second density peak δ_2 is the first and largest oscillatory period for the density profile. Various data from different literature are collected to illustrate the one molecular periodic density profile, as shown in Fig. 10.

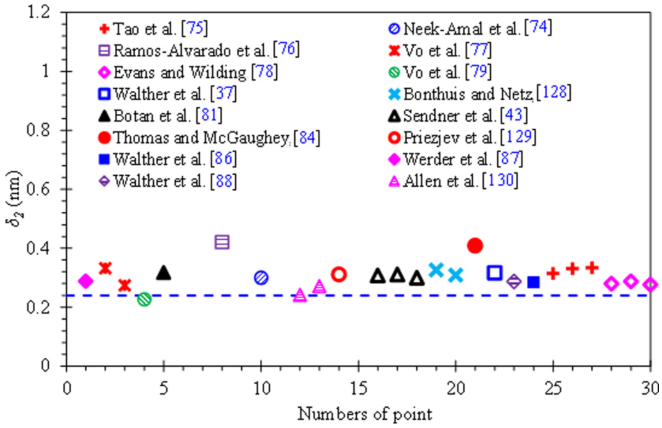

FIG. 10. Determination of the distance between the location of the first density peak and the second density peak δ_2. The data are from MD simulations in the literature, and the simulated wall surfaces are (1) flexible and rigid CNTs with various surface wettability (Tao *et al.* [85]); (2) flat walls with two graphene layers (Neek-Amal *et al.* [74]); (3) Si(111) plane (Ramos-Alvarado *et al.* [76]); (4) Cu and graphene-coated Cu surface wall (Vo *et al.* [77]); (5) Lennard-Jones hydrophobic substrate (Evans and Wilding [78]); (6) Au surface wall (Vo *et al.* [79]); (7) double-walled carbon nanotubes (DWCNTs) (Walther *et al.* [37]); (8) self-assembled monolayers consisting of single membranes of either $C_{20}H_{41}OH$ or $C_{20}H_4$ (Bonthuis and Netz [S10]); (9) sodium-saturated Wyoming montmorillonite surface to represent clay (Botan *et al.* [81]); (10) hydrophobic hydrogen terminated diamond surface (Sendner *et al.* [43]); (11) armchair CNTs (Thomas and McGaughey [84]); (12) two (111) planes with an FCC lattice consisting of 12,288 molecules (Priezjev *et al.* [129]); (13) zigzag CNTs (Walther *et al.* [86]); (14) CNTs (Werder *et al.* [87]); (15) CNTs (Walther *et al.* [88]); (16) Lennard-Jones hydrophobic and hydrophilic walls (Allen *et al.* [130]). The blue dashed line with the value of 0.28 nm is drawn to guide the reader's eyes.

Numerous molecular dynamics (MD) simulations have shown that, at a given water-solid pair and thermodynamic state, the periodically oscillated density profiles in nanochannels are independent of the external force [19,131], channel width [23,90], and temperature [68]. Specifically, even when the density peaks decay to nearly the value of bulk water, the periodic wavelength does not change [68].

APPENDIX D: CRITICAL PARAMETER IN MEAN-FIELD BODY FORCE EQUATION

The original Shan-Chen model was proposed in the application to simulate the multicomponent/phases problems, and the model supports phase transitions [132]. To avoid the phase transition in simulating single water phase flow in a confined situation, the parameter G_b should be tuned above the critical value $G_{b,c}$. To calculate $G_{b,c}$, we set the first and the second derivatives of the equation of state [Eq. (D1)] equal to zero

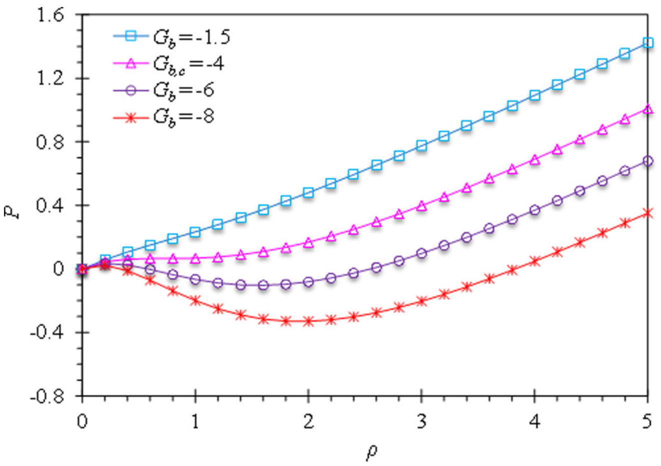

FIG. 11. P-ρ plot of the Shan-Chen equations of state. Dashed horizontal line is at $P = 0$.

[133]

$$p = c_s^2\rho + \frac{c_s^2 G_b}{2}\psi^2, \tag{D1}$$

where the phenomenological pseudopotential $\psi(x, t)$ is defined as

$$\psi(x, t) = 1 - \exp(-\rho/\rho_0). \tag{D2}$$

First and second derivatives of Eq. (D1) are

$$\frac{\partial p}{\partial \rho} = c_s^2 + c_s^2 G_{b,c}[1 - \exp(-\rho_c)]\exp(-\rho_c) = 0, \tag{D3}$$

$$\frac{\partial^2 p}{\partial \rho^2} = -c_s^2 G_{b,c}[1 - \exp(-\rho_c)]\exp(-\rho_c) + c_s^2 G_{b,c}\exp(-\rho_c)\exp(-\rho_c) = 0, \tag{D4}$$

where the subscript c denotes the critical state. Solving Eqs. (D3) and (D4), we calculated $G_{b,c} = -4$. The pressure (P) versus (ρ) diagram of these Shan-Chen equations of state is shown in Fig. 11. As shown in Fig. 11, the coexisting densities of the liquid water and vapor valishes when $G_b > -4$. Actually, G_b can be set with any value larger than the critical value -4; however, too large of this value may cause numerical instabilities due to the steep density gradients. In this work, we set $G_b = -1.5$ according to the suggestion in Harting *et al.* [134].

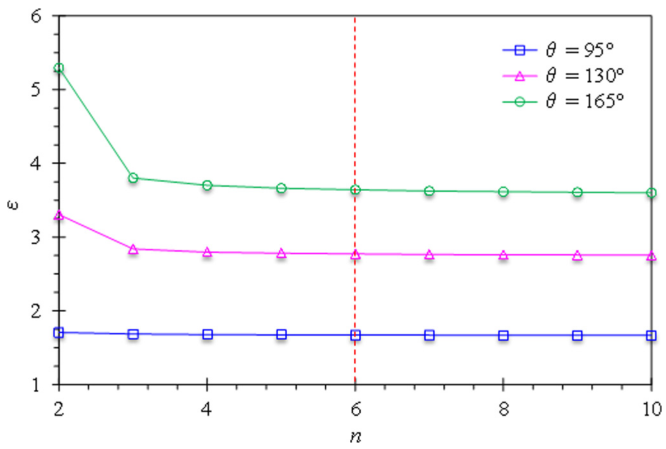

FIG. 12. Relationship between enhancement factors and n under different contact angles ($d = 2.034$ nm).

APPENDIX E: GRIDS OF THE TWO WATER BATHS

Theoretically, $n \rightarrow \infty$ is required to represent the two water baths, whereas it is computationally impossible and unnecessary to choose a very large n. From the figure, when n is larger than 6, the calculated enhancement factor tends to be stable, which means the two cavities are large enough to capture the bending of the streamlines, as shown in Fig. 12. Therefore, for all simulations, n is set at 6 to balance the computation cost and accuracy.

APPENDIX F: A SUMMARY OF VARIOUS PARAMETERS USED TO REPRODUCE FIGS. 2, 4, 7, 9, AND 10

A summary of various parameters used to reproduce Figs. 2(b), 9, and 10 is shown in Table II, to reproduce Fig. 4 is shown in Table III, and to reproduce Fig. 7 is shown in Table IV.

---

[1] M. A. Shannon, P. W. Bohn, M. Elimelech, J. G. Georgiadis, B. J. Mariñas, and A. M. Mayes, Nature **452**, 301 (2008).

[2] A. Siria, P. Poncharal, A.-L. Biance, R. Fulcrand, X. Blase, S. T. Purcell, and L. Bocquet, Nature **494**, 455 (2013).

[3] Y. Cui, Science **293**, 1289 (2001).

[4] J. Geng, K. Kim, J. Zhang, A. Escalada, R. Tunuguntla, L. R. Comolli, F. I. Allen, A. V. Shnyrova, K. R. Cho, D. Munoz *et al.*, Nature **514**, 612 (2014).

[5] F. Javadpour, M. Mcclure, and M. Naraghi, Fuel **160**, 549 (2015).

[6] J. Cui, Q. Sang, Y. Li, C. Yin, Y. Li, and M. Dong, Fuel **202**, 426 (2017).

[7] N. Pérez-Hernández, T. Q. Luong, M. Febles, C. Marco, H.-H. Limbach, M. Havenith, C. Pérez, M. V. Roux, R. Pérez, and J. D. Martín, J. Phys. Chem. C **116**, 9616 (2012).

[8] T. Zhang, X. Li, J. Shi, Z. Sun, Y. Yin, K. Wu, J. Li, and D. Feng, Chem. Eng. Sci. **187**, 280 (2018).

[9] S. K. Kannam, P. J. Daivis, and B. Todd, MRS Bull. **42**, 283 (2017).

[10] M. Majumder, N. Chopra, and B. J. Hinds, ACS Nano **5**, 3867 (2011).

[11] T. Werder, J. H. Walther, R. L. Jaffe, T. Halicioglu, F. Noca, and P. Koumoutsakos, Nano Lett. **1**, 697 (2001).

[12] N. E. Levinger. Science **298**, 1722 (2002).

[13] B. D. Todd, D. J. Evans, and P. J. Daivis, Phys. Rev. E **52**, 1627 (1995).
[14] L. F. Scatena, Science **292**, 908 (2001).
[15] D. Ortiz-Young, H.-C. Chiu, S. Kim, K. Voïtchovsky, and E. Riedo, Nat. Comm. **4**, 2482 (2013).
[16] L. Fu, S. Merabia, and L. Joly, J. Phys. Chem. Lett **9**, 2086 (2018).
[17] Y. Yin, Z. Qu, T. Zhang, J. Zhang, and Q. Wang, Fuel **273**, 117750 (2020).
[18] S. K. Kannam, B. D. Todd, J. S. Hansen, and P. J. Daivis, J. Chem. Phys. **138**, 094701 (2013).
[19] W. Lei, M. K. Rigozzi, and D. R. Mckenzie, Rep. Prog. Phys. **79**, 025901 (2016).
[20] K. P. Travis, B. D. Todd, and D. J. Evans, Phys. Rev. E **55**, 4288 (1997).
[21] K. Falk, B. Coasne, R. Pellenq, F.-J. Ulm, and L. Bocquet, Nat. Comm. **6**, 6949 (2015).
[22] M. K. Borg and J. M. Reese, MRS Bull. **42**, 294 (2017).
[23] M. E. Suk and N. R. Aluru, RSC Adv. **3**, 9365 (2013).
[24] J. Ghorbanian and A. Beskok, Microfl. Nanofl. **20**, 121 (2016).
[25] K. Ritos, D. Mattia, F. Calabrò, and J. M. Reese, J. Chem. Phys. **140**, 014702 (2014).
[26] A. A. Pahlavan and J. B. Freund, Phys. Rev. E **83**, 021602 (2011).
[27] Y. Zhang, Int. J. Heat Mass Trans. **100**, 295 (2016).
[28] W. Chen, R. Zhang, and J. Koplik, Phys. Rev. E **89**, 023005 (2014).
[29] N. Rajabbeigi, B. Elyassi, T. T. Tsotsis, and M. Sahimi, J. Membrane Sci. **335**, 5 (2009).
[30] N. Rajabbeigi, T. T. Tsotsis, and M. Sahimi, J. Membrane Sci. **345**, 323 (2009).
[31] S. Naserifar, W. A. Goddard, L. Liu, T. T. Tsotsis, and M. Sahimi, J. Phys. Chem. C **117**, 3320 (2013).
[32] S. Naserifar, T. T. Tsotsis, W. A. G. Iii, and M. Sahimi, J. Membrane Sci. **473**, 85 (2015).
[33] S. Naserifar, W. A. Goddard, T. T. Tsotsis, and M. Sahimi, J. Chem. Phys. **142**, 174703 (2015).
[34] M. Firouzi and M. Sahimi, Transport Porous Med. **115**, 495 (2016).
[35] J. K. Holt, Science **312**, 1034 (2006).
[36] K. Ritos, M. K. Borg, D. A. Lockerby, D. R. Emerson, and J. M. Reese, Microfl. Nanofl. **19**, 997 (2015).
[37] J. H. Walther, K. Ritos, E. R. Cruz-Chu, C. M. Megaridis, and P. Koumoutsakos, Nano Lett. **13**, 1910 (2013).
[38] J. A. Thomas, A. J. Mcgaughey, and O. Kuter-Arnebeck, Int. J. Therm. Sci. **49**, 281 (2010).
[39] D. Feng, X. Li, X. Wang, J. Li, T. Zhang, Z. Sun, M. He, Q. Liu, J. Qin, and S. Han, Chem. Eng. Sci. **186**, 228 (2018).
[40] P. L. Bhatnagar, E. P. Gross, and M. Krook, Phys. Rev. **94**, 511 (1954).
[41] Y. H. Qian, D. Dhumières, and P. Lallemand, Europhys. Lett. **17**, 479 (1992).
[42] M. Majumder, N. Chopra, R. Andrews, and B. Hinds, Nature **438**, 44 (2005).
[43] C. Sendner, D. Horinek, L. Bocquet, and R. R. Netz, Langmuir **25**, 10768 (2009).
[44] P. A. Thompson and M. O. Robbins, Science **250**, 792 (1990).
[45] A. Koklu, J. Li, S. Sengor, and A. Beskok, Microfl. Nanofl. **21**, 124 (2017).
[46] U. Heinbuch and J. Fischer, Phys. Rev. A **40**, 1144 (1989).
[47] J.-L. Barrat and L. Bocquet, Phys. Rev. Lett. **82**, 4671 (1999).
[48] O. I. Vinogradova, K. Koynov, A. Best, and F. Feuillebois, Phys. Rev. Lett. **102**, 118302 (2009).
[49] T. Zhang, X. Li, Z. Sun, D. Feng, Y. Miao, P. Li, and Z. Zhang, Chem. Eng. Sci. **174**, 1 (2017).
[50] J. N. Israelachvili, *Intermolecular and Surface Forces* (Elsevier, Amsterdam, 2011).
[51] K. Wu, Z. Chen, J. Li, X. Li, J. Xu, and X. Dong, Proc. Nat. Acad. Sci. USA **114**, 3358 (2017).
[52] L. Chen, Q. Kang, Y. Mu, Y. L. He, and W. Q. Tao, Int. J. Heat Mass Trans. **76**, 210 (2014).
[53] Z. Chai, Z. Guo, L. Zheng, and B. Shi, J. App. Phys. **104**, 014902 (2008).
[54] S. Sauro, Phys. Rev. Lett. **89**, 064502 (2002).
[55] J. C. Maxwell, Phil. Trans. Royal Soc. London **170**, 231 (1979).
[56] Z. Chai, B. Shi, and Z. Guo, Commun. Comput. Phys. **8**, 1052 (2010).
[57] K. Wang, Z. Chai, G. Hou, W. Chen, and S. Xu, Comput. Fluids **161**, 60 (2018).
[58] Z. Guo, B. Shi, T. S. Zhao, and C. Zheng, Phys. Rev. E **76**, 056704 (2007).
[59] S. Granick, Y. Zhu, and H. Lee, Nat. Mat. **2**, 221 (2003).
[60] K. Wu, Z. Chen, J. Li, J. Xu, K. Wang, S. Wang, X. Dong, Z. Zhu, Y. Peng *et al.*, Angewandte Chemie Int. Ed. **57**, 8432 (2018).
[61] D. A. Doshi, E. B. Watkins, J. N. Israelachvili, and J. Majewski, Proc. Nat. Acad. Sci. USA **102**, 9458 (2005).
[62] P. A. Thompson and S. M. Troian, Nature **389**, 360 (1997).
[63] A. P. Bowles and W. A. Ducker, J. Phys. Chem. C **117**, 14007 (2013).
[64] K. Ahmad, X. Zhao, Y. Pan, W. Wang, and Y. Huang, J. Phys. Chem. C **119**, 12531 (2015).
[65] V. S. Craig, C. Neto, and D. R. Williams, Phys. Rev. Lett. **87**, 054504 (2001).
[66] D. M. Huang, C. Sendner, D. Horinek, R. R. Netz, and L. Bocquet, Phys. Rev. Lett. **101**, 226101 (2008).
[67] D. Y. C. Chan and R. G. Horn, J. Chem. Phys. **83**, 5311 (1985).
[68] A. E. Giannakopoulos, F. Sofos, T. E. Karakasidis, and A. Liakopoulos, Microfl. Nanofl. **17**, 1011 (2014).
[69] J. Ghorbanian, A. T. Celebi, and A. A. Beskok, J. Chem. Phys. **145**, 184109 (2016).
[70] P. Wu, A. Nikolov, and F. Wasan, Adv. Coll. Interf. Sci. **243**, 114 (2017).
[71] R. Bhadauria, T. Sanghi, and N. R. Aluru, J. Chem. Phys. **143**, 174702 (2015).
[72] F. Kerstin, S. Felix, J. Laurent, R. R. Netz, and B. Lydéric, Langmuir: ACS J. Surf. Coll. **28**, 14261 (2012).
[73] L. Bocquet and J. L. Barrat, Phys. Rev. E **49**, 3079 (1994).
[74] M. Neek-Amal, F. M. Peeters, I. V. Grigorieva, and A. K. Geim, ACS Nano **10**, 3685 (2016).
[75] J. Tao, X. Song, T. Zhao, S. Zhao, and H. Liu, Chem. Eng. Sci. **192**, 1252 (2018).
[76] B. Ramos-Alvarado, S. Kumar, and G. P. Peterson, Phys. Rev. E **93**, 033117 (2016).
[77] T. Q. Vo and B. H. Kim, Sci. Rep. **6**, 33881 (2016).
[78] R. Evans and N. B. Wilding, Phys. Rev. Lett. **115**, 016103 (2015).

[79] T. Q.Vo, M. Barisik, and B. H. Kim, Phys. Rev. E **92**, 053009 (2015).

[80] H. Hu, B. Luyao, and H. Suhe, Chinese J. Theor. & Appl. Mech. **45**, 507 (2013).

[81] A. Boţan, B. Rotenberg, V. Marry, and P. Turq, J. Phys. Chem. C **115**, 16109 (2011).

[82] A. Alexiadis and S. Kassinos, Chem. Eng. Sci. **63**, 2793 (2015).

[83] X. Chen, Molecular dynamics simulation of nanochannel flow, Doctoral thesis, University of Science and Technology of China, 2008.

[84] J. A. Thomas and A. J. H. McGaughey, J. Chem. Phys. **128**, 084715 (2008).

[85] H. Xiang, J. Eng. Thermophys. **18**, 1346 (2008).

[86] J. H. Walther, T. Werder, R. L. Jaffe, and P. Koumoutsakos, Phys. Rev. E **69**, 062201 (2004).

[87] T. Werder, J. H. Walther, R. L. Jaffe, T. Halicioglu, and T. Koumoutsakos, J. Phys. Chem. B **107**, 1345 (2003).

[88] J. H. Walther, R. Jaffe, T. Halicioglu, and P. Koumoutsakos, and P. J, Phys. Chem. B **105**, 9980 (2001).

[89] D. Feng, X. Li, X. Wang, J. Li, T. Zhang, Z. Sun, M. He, Q. Liu, J. Qin, and S. Han *et al.*, Langmuir: ACS J. Surf. Coll. **34**, 7714 (2018).

[90] G. Cicero, J. C. Grossman, E. Schwegler, F. Gygi, and G. Galli, J. Am. Chem. Soc. **130**, 1871 (2008)..

[91] M. Neekamal, A. Lohrasebi, M. Mousaei, F. Shayeganfar, B. Radha, and F. M. Peeters, Appl. Phys. Lett. **113**, 083101 (2018).

[92] X. Shan and H. Chen, Phys. Rev. E **49**, 2941 (1994).

[93] J. Zhang and D. Y. Kwok, Phys. Rev. E **70**, 056701 (2004).

[94] R. Benzi, L. Biferale, M. Sbragaglia, S. Succi, and F. Toschi, Europhys. Lett. **74**, 651(2006).

[95] X. Shan and H. Chen, Phys. Rev. E **47**, 1815 (1993).

[96] R. S. Voronov, D. V. Papavassiliou, and L. L. Lee, Ind. Eng. Chem. Res. **47**, 2455 (2008).

[97] S. Gruener, D. Wallacher, S. Greulich, M. Busch, and P. Huber, Phys. Rev. E **93**, 013102 (2016).

[98] J. A. Thomas and A. J. H. Mcgaughey, Phys. Rev. Lett. **102**, 184502 (2009).

[99] E. Secchi, S. Marbach, A. Niguès, D. Stein, A. Siria, and L. Bocquet, Nature **537**, 210 (2016).

[100] K. P. Lee, H. Leese, and D. Mattia, Nanoscale **4**, 2621 (2012).

[101] M. Whitby, L. Cagnon, M. Thanou, and N. Quirke, Nano Lett. **8**, 2632 (2008).

[102] S. Sinha, M. P. Rossi, D. Mattia, Y. Gogotsi, and H. H. Bau, Phys. Flu. **19**, 013603 (2007).

[103] E. Chiavazzo, M. Fasano, P. Asinari, and P. Decuzzi, Nat. Comm. **5**, 3565 (2014).

[104] A. A. Milischuk and B. M. Ladanyi, J. Chem. Phys. **135**, 174709 (2011).

[105] J. S. Babu and S. P. Sathian, J. Chem. Phys. **134**, 194509 (2011).

[106] J. A. Thomas and A. J. Mcgaughey, Nano Lett. **8**, 2788 (2008).

[107] S. Joseph and N. R. Aluru, Nano Lett. **8**, 452 (2008).

[108] M. E. Suk and N. R. Aluru, Nanosc. Microsc. Therm. **21**, 247 (2017).

[109] T. B. Sisan and S. Lichter, Microfl. Nanofl. **11**, 787 (2011).

[110] K. Wu, Z. Chen, J. Li, J. Xu, K. Wang, R. Li, S. Wang, and X. Dong, Langmuir **35**, 8867 (2019).

[111] S. Gravelle, L. Joly, F. Detcheverry, C. Ybert, C. Cottin-Bizonne, and L. Bocque, Proc. Natl. Acad. Sci. USA **110**, 16367 (2013).

[112] K. S. Glavatskiy and S.K. Bhatia, Langmuir **32**, 3400 (2016).

[113] L. Wang, R. S. Dumont, and J. M. Dickson, J. Chem. Phys. **137**, 044102 (2012).

[114] A. Popadić, J. H. Walther, P. Koumoutsakos, and M. Praprotnik, New J. Phys. **16**, 082001 (2014).

[115] M. Sbragaglia, R. Benzi, L. Biferale, and S. Succi, and F. Toschi, Phys. Rev. Lett. **97**, 204503 (2006).

[116] Z. Guo and C. Shu, *Lattice Boltzmann Method and Its Applications in Engineering* (World Scientific, Singapore, 2013).

[117] T. Krüger, H. Kusumaatmaja, and A. Kuzmin, *The Lattice Boltzmann Method: Principles and Practice* (Springer, Switzerland, 2017).

[118] I. S. Anastasios, M. A. David, J. J Karl, and S. S. David, Phys. Rev. Lett. **89**, 185901 (2002).

[119] B. Ramos-Alvarado, S. Kumar, and G. P. Peterson, App. Phys. Lett. **108**, 074105 (2016).

[120] J. Li, Z. Chen, K. Wu, T. Zhang, R. Zhang, J. Xu, R. Li, S. Qu, J. Shi, and X. Li, AIChE J. **64**, 3529 (2018).

[121] A. Afsharpoor and F. Javadpour, Fuel **180**, 580 (2016).

[122] Z. Yu and L. S. Fan, J. Comp. Phys. **228**, 6456 (2009).

[123] X. He, Q. Zou, L. S. Luo, and M. Dembo, J. Stat. Phys. **87**, 115 (1997).

[124] S. Succi, *The Lattice Boltzmann Equation – for Fluid Dynamics and Beyond* (Oxford University Press, Oxford, UK, 2017).

[125] H. Yoshida and L. Bocquet, J. Chem. Phys. **144**, 234701 (2016).

[126] M. Shaat, Langmuir: ACS J. Surf. Coll. **33**, 12814 (2017).

[127] G. J. Wang and N. G. Hadjiconstantinou, Phys. Flu. **27**, 052006 (2015).

[128] D. J. Bonthuis and R. R. Netz, J. Phys. Chem. B **117**, 11397 (2013).

[129] N. V. Priezjev, A. A. Darhuber, and S. M. Troian, Phys. Rev. E **71**, 041608 (2005).

[130] T. W. Allen, S. Kuyucak, and S. H. Chung, J. Chem. Phys. **111**, 7985 (1999).

[131] D. T. Semiromi and A. R. Azimian, Heat Mass Transfer **46**, 791 (2010).

[132] M. C. Sukop and D. T. T. Jr, *Lattice Boltzmann Modeling: An Introduction for Geoscientists and Engineers* (Springer Publishing Company, Berlin, 2010).

[133] H. Huang, M. Sukop, and X. Lu, *Multiphase Lattice Boltzmann Method Theory and Application* (Wiley Blackwell, Hoboken, NJ, 2015).

[134] J. Harting, C. Kunert, and H. J. Herrmann, Europhys. Lett. **75**, 328 (2005).